

High performance control of mirror segment actuators for the European Extremely Large Telescope

Gert Witvoet^a, Remco den Breeje^a, Jan Nijenhuis^a, René Hazelebach^a and Niek Doelman^a

^aTNO Technical Sciences, Opto-Mechatronics department,
Stieltjesweg 1, 2628 CK Delft, The Netherlands

ABSTRACT

Segmented primary mirror telescopes require dedicated piston-tip-tilt actuators for optimal optical performance. TNO has developed various prototypes of such actuators, in particular for the E-ELT. In this paper the control results of a specific two-stage prototype will be presented. First, the dynamics of the actuator in interconnection with the to-be-positioned mass has been analyzed, both using frequency response measurements and first principles modeling, resulting in a detailed understanding of the dynamic behavior of the system. Next, feedback controllers for both the fine and the coarse stage have been designed and implemented. Finally, the feedback-controlled actuator has been subjected to a realistic tracking experiment; the results have demonstrated that the TNO actuator is able to suppress wind force disturbances and ground vibrations with more than a factor 10^3 , down to 1.4 nm RMS, which is compliant with the requirements.

Keywords: E-ELT, M1 segmented mirror, position actuator, feedback control, tracking

1. INTRODUCTION

Future extremely large telescopes, such as the Thirty Meter Telescope (TMT), the Giant Magellan Telescope (GMT) and the European Extremely Large Telescope (E-ELT), will be equipped with segmented primary mirrors (M1). The feasibility of a segmented M1 concept has successfully been demonstrated on the Keck¹ telescopes; other telescopes with segmented primary mirrors such as HET, SALT and GTC later followed the Keck example.

To achieve optimal optical performance in such a concept each individual mirror segment of the M1 should be actively controlled in at least the rigid-body piston-tip-tilt movements. To this extend each segment can be equipped with three dedicated single-DOF actuators. These piston-tip-tilt actuators, often called PACT (Position ACTuator), should combine ultra-high accuracy with a relatively large stroke, while being exposed to non-stationary structural vibrations and wind loads.

Over the last couple of years TNO has designed and realized various different PACT prototypes for the E-ELT. In 2007 TNO already delivered 18 Wind Experiment Breadboard (WEB) PACTs² to ESO. In the last two years TNO has developed follow-up prototypes which are compliant with updated requirements, regarding e.g. reduced dimensions and power consumption and increased performance. These recent prototypes are intentionally mutually different and vary in various aspects. As such experience has been gained with various coarse stage actuators (stepper motor vs brushless DC-motor), spindle types, and lateral supports. Each prototype has been extensively tested in a dedicated test setup, in the presence of ground vibrations and realistic wind disturbances, both in stand-still and in tracking configuration, and their performance has been assessed in relation to the requirements. A detailed discussion on the prototype differences is outside the scope of this article; instead, the results of a specific prototype will be discussed, which is a DC-motor driven PACT with an elastic lateral support. This performance assessment includes a detailed discussion on the dynamics of PACT in its setup, the controller design and final performance measurements.

2. SYSTEM DESCRIPTION

Before continuing to the analysis and controller design, the section will briefly summarize the actuator concept and the test setup in which PACT has been qualified.

Further author information:

G. Witvoet: E-mail: Gert.Witvoet@tno.nl, Telephone: +31 (0) 888 666 483

Ground-based and Airborne Telescopes V, edited by Larry M. Stepp, Roberto Gilmozzi,
Helen J. Hall, Proc. of SPIE Vol. 9145, 91451S • © 2014 SPIE
CCC code: 0277-786X/14/\$18 • doi: 10.1117/12.2056901

Proc. of SPIE Vol. 9145 91451S-1



Figure 1: Picture of one of the recent PACT prototypes. Photo: TNO / Fred Kamphues.

2.1 The actuator

The recent PACT prototypes have been designed with the following key requirements³ in mind:

- Axial load on an individual actuator: between 0 and 900 N
- Orientation: between 0° and 90°
- PACT should have its own internal metrology
- Tracking velocity: up to 1.2 $\mu\text{m/s}$
- Tracking accuracy: 1.7 nm RMS on the internal metrology
- Total stroke: 15 mm
- Maximum power dissipation during tracking: less than 1 W
- Series production cost price: less than 4000 euro

To be able to meet the combination of large stroke and high accuracy the PACT prototypes have been designed as two-stage actuators. To enable high accuracy a voice coil has been selected for the fine stage (soft actuator principle). To achieve the 15 mm stroke and to minimize power consumption, this fine stage is off-loaded via a coarse stage actuator. Experience has been gained with both a stepper motor and brushless DC-motor; in this article only the DC-motor results will be discussed.

PACT also comprises a set of internal springs to off-load the varying gravity force up to 900 N, which comes with the changing orientation of the mirror segment assembly. To comply with the lateral stiffness requirement, to withstand non-axial loads, PACT is equipped with a lateral support. Both a sliding bearing and an elastic support has been assessed; the results in this article relate to the PACT with the elastic support. Moreover, every PACT prototype has a commercial on-axis nanometer resolution encoder close to the tip of the actuator; this internal metrology will be used as the feedback signal later on. Overall, PACT has been designed with as many commercial off-the-shelf components and easy-to-manufacture parts as possible, to keep the cost price low. A picture of one of the prototypes is shown in figure 1.

2.2 The test setup

To assess the dynamics and performance of PACT in relation to the load it is required to actuate, PACT has been mounted in a special test setup. A part of this setup is visible in figure 2, next to a schematic drawing. The base of PACT is mounted to a heavy box (of around 150 kg), which represents the fixed frame of the M1 support structure plus a part of the M1 back structure. Inside this box is a 90 kg test mass, guided by some low-stiffness

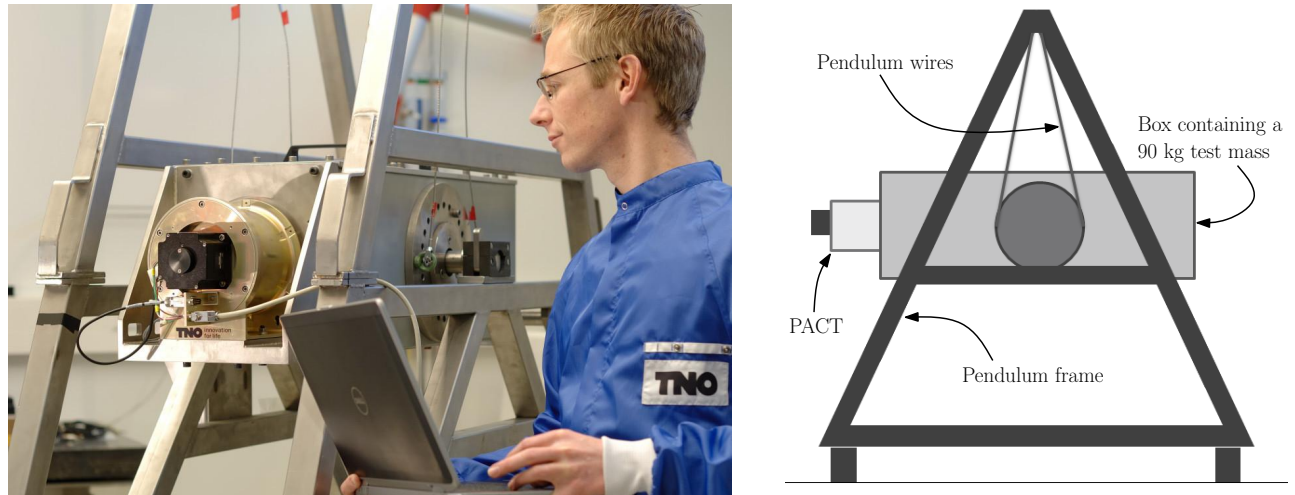


Figure 2: Picture and schematic drawing of the PACT test setup. The actuator displayed in the picture is the one with the stepper motor. Photo: TNO / Fred Kamphues.

leaf springs, representing the required load which has to be actuated. Between this test mass and PACT is a carefully designed strut, which has a stiffness matching the M1 support structure stiffness as experienced by a single PACT.

This complete assembly is hanging on pendulum wires (with relatively low stiffness) so that the box can freely oscillate. As such high-frequency ground vibrations are passively attenuated. Reason for this approach is that the ground vibration level in the TNO laboratory where the setup is situated is quite high; by passively attenuating this spectrum a more realistic input disturbance spectrum can be obtained, i.e. more representative for the disturbances present on the E-ELT site. The angle between the box and the horizontal plane, which is labeled β , can be varied statically (in figure 2 the angle is 0°), thereby facilitating measurements under various PACT orientations and thus varying gravitational loads.

3. SYSTEM IDENTIFICATION

A proper controller design should always start with the identification of the dynamics of the to-be-controlled system. A natural and fast way of doing this is via frequency response function (FRF) measurements. This section will discuss some FRF results, followed by the derivation of a first-principles model to explain the observed dynamics.

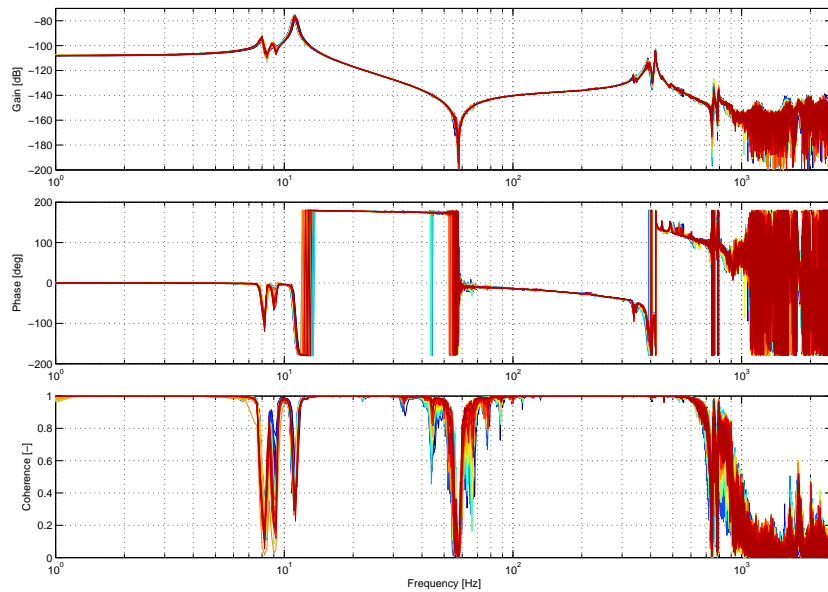
3.1 Frequency response measurements

When measuring the frequency response of the overall system (i.e. PACT in its test setup) only the fine stage is considered, since this is the stage which should eventually meet the accuracy requirement. Proper controller design is crucial for this stage, which relies on accurate fine stage FRFs.

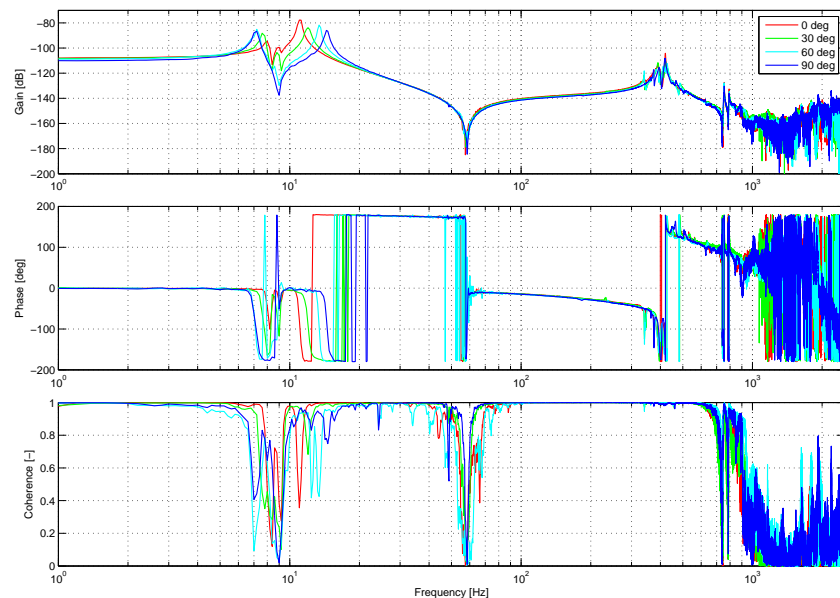
The FRFs are obtained in open loop by perturbing the fine stage around various nominal operating points. To this end the PACT angle β and the coarse stage position are fixed, and then a certain amount of low-pass filtered noise w is added to the voice coil input. The resulting displacement y on the internal sensor is measured, so that the local FRF can be calculated from the ratio between the cross-power density S_{yw} and auto-power density S_{ww} of the two signals, i.e.

$$H_i(j\omega) = \frac{S_{yw}(j\omega)}{S_{ww}(j\omega)}, \quad (1)$$

which is valid around its nominal operating point i . By repeating this measurement for different operating points, i.e. for different angles β and coarse stage positions, a set of FRFs can be obtained which demonstrate the dependence of the dynamics on the operating point.



(a) As a function of the coarse stage position (in horizontal configuration); dark blue is fully retracted, dark red is fully extracted.



(b) As a function of the angle of PACT with the horizontal plane; note that the low-frequent modes around 10 Hz change significantly.

Figure 3: Measured FRFs of PACT in connection to the test mass.

The FRF measurements are summarized in figure 3, using 180 s of measurement data per FRF and a resolution of 0.2 Hz. In figure 3(a) the PACT angle is fixed at $\beta = 0^\circ$ (horizontal position) and the position of the coarse stage is varied over its total stroke of 15 mm. It can be seen that the FRFs are nearly identical, which proves that the fine stage dynamics are hardly dependent on the coarse stage. The very minor differences can be allocated to minor changes in the effective mass and stiffness as experienced by the fine stage, since the coarse stage essentially alters the ‘length’ of the actuator. The great resemblance will simplify the controller design and will

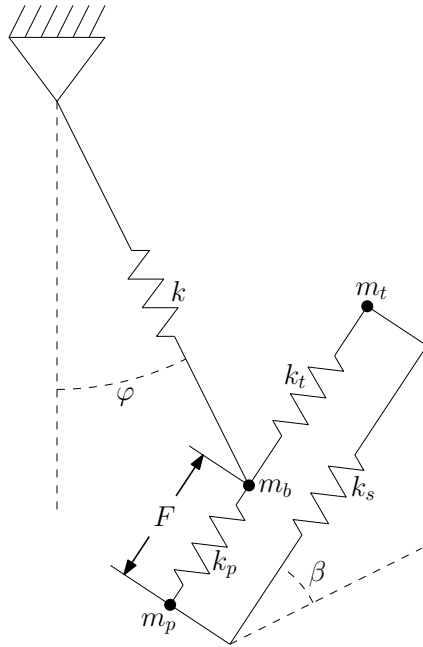


Figure 4: Schematic representation of PACT in its test setup.

enable good performance over the complete stroke of the actuator.

Figure 3(b) depicts the FRFs as a function of the PACT angle β , while the position of the coarse stage is fixed to the neutral middle position of 0 mm. Surprisingly, there is a large dependency of the low-frequent eigenmodes on the PACT angle. However, it was realized that this non-linear effect could be caused by either PACT itself, or the test setup in which it hangs. The FRFs cannot discriminate between these two, therefore it has been decided to assess the change in dynamic behavior of PACT in connection to a to-be-positioned mass (be it a test mass or an M1 segment) via the derivation of an analytic model based on first principles.

3.2 First principles modeling

The derivation of the analytic model has started with a schematic representation of the overall system, which is shown in figure 4. The model contains three masses, i.e. the moving mass of PACT m_p , the test mass m_t and the mass of the surrounding box (including the non-moving part of PACT) m_b . These masses are interconnected via the stiffness of the PACT internal springs k_p , a strut stiffness k_s (representing the stiffness of the eventual M1 segment support), and the stiffness of the linear guidance of the test mass k_t . The box is suspended via the pendulum wire stiffness k to the frame, which in this model represents the fixed world. The nominal length of the pendulum is labeled L , while δ_p and δ_t denote the off-loaded nominal distance between m_p and m_b , and m_b and m_t respectively. The angle β which the box makes with respect to the normal of the pendulum is a fixed but tunable parameter; in the test setup $-180^\circ \leq \beta \leq 180^\circ$ with steps of 15° .

The model has four degrees of freedom (DOF) which can fully describe the motion of the system, namely

- x_p : elongation of the PACT springs k_p
- x_t : elongation of the test mass guidance k_t
- y : elongation of the pendulum k
- φ : rotation of the pendulum.

These DOF fully define the vertical and horizontal motion of all masses, as shown in Appendix A. The equations of motion can be derived using Lagrange's method,⁴ which is based on expressions of the kinetic energy T , potential energy V and non-conservative forces Q^{nc} :

$$\frac{d}{dt} (T, \dot{q}) - T, q + V, q = (Q^{nc})^T, \quad (2)$$

where $X_{,z}$ denotes the partial derivative of X with respect to z . The total kinetic energy of the system is defined by the velocity of the masses, i.e.

$$T = \frac{1}{2}m_b v_{\text{box}}^2 + \frac{1}{2}m_p v_{\text{PACT}}^2 + \frac{1}{2}m_t v_{\text{testmass}}^2, \quad (3)$$

whereas the total potential energy, defined by the springs and the gravitational field, is given by

$$V = \frac{1}{2}ky^2 + \frac{1}{2}k_p x_p^2 + \frac{1}{2}k_t x_t^2 + \frac{1}{2}k_s (x_p - x_t)^2 + m_b g y_{\text{box}} + m_p g y_{\text{PACT}} + m_t g y_{\text{testmass}}. \quad (4)$$

The actuator force F is co-located with x_p , so that Q^{nc} is simply $Q^{nc} = [F, 0, 0, 0]$. By writing T and V in terms of the generalized DOF, linearizing the expressions around the zero position (i.e. assuming only small rotations φ), calculating the appropriate partial derivatives and substituting the results into (2), we then obtain the undamped equations of motion

$$M\ddot{q} + Kq = Qu, \quad (5)$$

where q is the vector of generalized DOF and the input $u = F$. Moreover, $Q = [1, 0, 0, 0]^T$ and

$$M = \begin{bmatrix} m_p & 0 & -m_p \sin \beta & -m_p L \cos \beta \\ 0 & m_t & -m_t \sin \beta & -m_t L \cos \beta \\ -m_p \sin \beta & -m_t \sin \beta & m_b + m_p + m_t & -(m_p \delta_p - m_t \delta_t) \cos \beta \\ -m_p L \cos \beta & -m_t L \cos \beta & -(m_p \delta_p - m_t \delta_t) \cos \beta & (m_b + m_p + m_t)L^2 \\ & & & + (m_p \delta_p^2 + m_t \delta_t^2) \\ & & & + 2L(m_p \delta_p - m_t \delta_t) \sin \beta \end{bmatrix} \quad (6)$$

$$K = \begin{bmatrix} k_p + k_s & -k_s & 0 & -m_p g \cos \beta \\ -k_s & k_t + k_s & 0 & -m_t g \cos \beta \\ 0 & 0 & k & 0 \\ -m_p g \cos \beta & -m_t g \cos \beta & -(m_p \delta_p - m_t \delta_t) \cos \beta & (m_b + m_p + m_t)gL \\ & & & + g(m_p \delta_p - m_t \delta_t) \sin \beta \end{bmatrix}. \quad (7)$$

More details on the derivation of these matrices can be found in Appendix A. The undamped eigenfrequency matrix Λ and mode shapes Φ of this model can be found by solving the eigenvalue problem

$$K\Phi = M\Phi\Lambda, \quad (8)$$

with which modal damping can be defined and added to the system. As such we define

$$D = 2\zeta\sqrt{\Lambda}, \quad (9)$$

where ζ is the normalized damping ratio, so that the total model is given by

$$M\ddot{q} + D\dot{q} + Kq = Qu, \quad (10)$$

with M , D and K as defined in (6), (9) and (7) respectively. For control purposes it is useful to write this model in state-space form, where the system output z is the PACT internal sensor, which in this case corresponds to x_p . As such we obtain

$$\dot{x} = \begin{bmatrix} \mathbf{0} & I \\ -M^{-1}K & -M^{-1}D \end{bmatrix} x + \begin{bmatrix} \mathbf{0} \\ M^{-1}Q \end{bmatrix} u \quad (11a)$$

$$z = \begin{bmatrix} 1 & \mathbf{0} \end{bmatrix} x, \quad (11b)$$

where $x = [q, \dot{q}]^T$ and $u = F$.

The mass and stiffness parameters of the model have been taken from CAD drawings, and a modal damping of 1% has been used. The resulting frequency responses in figure 5 show a large resemblance to the FRF measurements in figure 3(b). For both the low-frequency anti-resonance remains steady at 9 Hz for changing β , while the two surrounding resonances move away from the anti-resonance as β increases. Moreover, the model nicely matches the DC-gain, the mass-line between 15 and 50 Hz, the anti-resonance at 60 Hz and the large resonance around 400 Hz. Hence, the model properly describes the global dynamic behavior, and can be used to assess the mode shapes of the system.

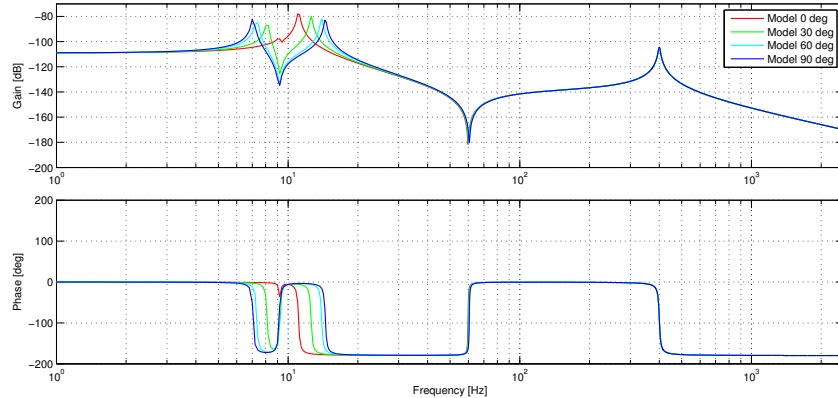


Figure 5: Frequency responses of the analytic model, as a function of β .

3.2.1 Mode shape interpretation

The modal analysis (8) returns the mode shapes Φ of the system, which have revealed that the 60 Hz anti-resonance and 400 Hz resonance correspond to the decoupling of the 90 kg test mass from the moving mass of PACT (1.32 kg); this mode is not influenced by the angle β . Moreover, there is a pendulum mode at 0.47 Hz, which cannot be excited by PACT and is therefore uncontrollable, and is also not influenced by β . When $\beta = 0^\circ$ the other two modes correspond to the resonance of the total mass on the pendulum wire stiffness k (around 8.7 Hz) and the resonance of the combined mass m_p and m_t with respect to the box m_b on the stiffnesses k_p and k_t (around 11.1 Hz). For $\beta = 0^\circ$ these modes are perpendicular, as the first is a pure vertical and the second a pure horizontal mode. Consequently, the vertical 8.7 Hz mode is nearly unobservable by the internal sensor when PACT is oriented horizontally. However, as β increases, the relative displacements of the masses will interact with the vertical mode and vice versa. Hence, the stiffnesses k_p and k_t will interact with k in the first resonance, and vice versa in the second. Since k is stiffer than k_p and k_t , the eigenfrequency of the first resonance will decrease and the one of the second will increase. Moreover, both modes become clearly observable by the internal sensor as β increases.

In essence, this analysis has revealed that the stiffness that the masses m_b , m_p and m_t ‘feel’ towards the fixed world, changes from the one of the swing motion (roughly $2 \cdot 10^3$ N/m) to the one of the pendulum wire $k = 7.2 \cdot 10^5$ N/m as β increases. This is clearly an artifact from the test setup. In an assembly with M1 and its support structure this is not likely to occur, since the stiffness to the fixed world in the direction of the actuator is approximately constant in that configuration.

For the rest of this paper we will restrict ourselves to the horizontal configuration only. Hence, the FRFs in figure 3(a) will be used in the controller design in Section 4.1.

3.3 Wind disturbance modeling

There are essentially two external disturbances which can limit the performance of a PACT: ground or frame vibrations from below, and wind forces from above. Ground vibrations are of course always present, and in case of the TNO laboratory these can be quite high. Apart from some passive isolation the ground vibrations are left as is; PACT will thus have to deal with the remaining error spectrum, which is roughly in the same order of magnitude as the expected spectrum for frame and/or ground vibrations on the E-ELT site.

Wind disturbances will have to be added artificially in a lab environment. To this end a force disturbance signal is added to the voice coil force. This disturbance signal is generated by filtering a random noise signal such that the output spectrum closely resembles the specified operational spectrum at the E-ELT site.⁵ According to these specifications the on-site wind velocity distribution $S_{uu}(f)$ can be modeled via a Von Karman model⁶

$$S_{uu}(f) = \frac{4I_u^2 V_z L_u}{\left(1 + 70.8 \left(\frac{L_u}{V_z} f\right)^2\right)^{5/6}}, \quad (12)$$

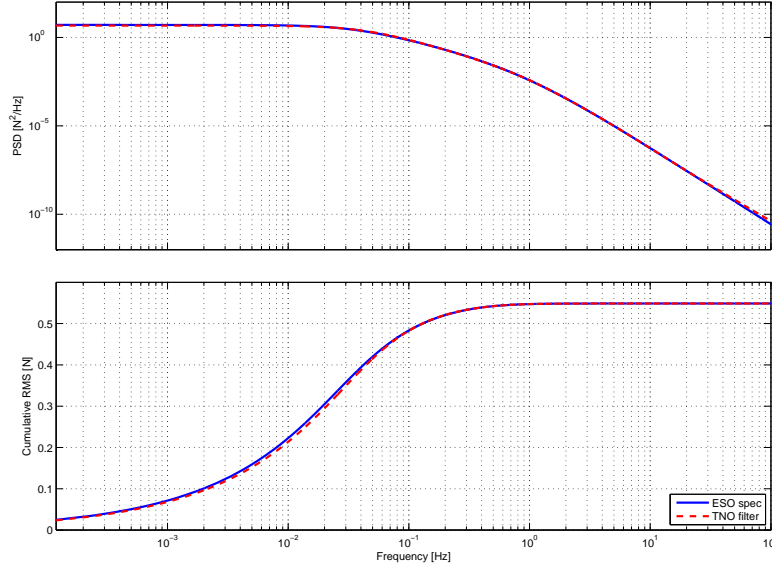


Figure 6: Specified wind force disturbance spectrum (15) on PACT level (solid blue), compared to the output spectrum of the linear filter used to simulate this wind force (dashed red). The bottom plot shows the corresponding cumulative RMS.

where the intensity of turbulence $I_u = 0.4$, the mean wind speed $V_z = 2$ m/s and the integral length scale of turbulence $L_u = 7$ m. This velocity spectrum can be converted to a force spectrum via the aerodynamic admittance function $\chi_a(f)$ defined as

$$\chi_a(f) = \frac{1}{1 + \left(2f \frac{\sqrt{A}}{V_z}\right)^{4/3}}, \quad (13)$$

where $A = 1.3$ m² is the area of an M1 segment, and the drag equation defined as

$$F = \frac{1}{2} \rho V_z^2 A C_d, \quad (14)$$

where the drag coefficient of a single segment is assumed to be $C_d = 1$ and the mass density of air is assumed to be $\rho = 0.87$ kg/m³ at the E-ELT site.⁵ The wind force distribution $S_{FF}(f)$ is then given by⁷

$$S_{FF}(f) = 4 \left(\frac{F}{V_z}\right)^2 \chi_a^2(f) \cdot S_{uu}(f). \quad (15)$$

Using the mentioned parameter values this yields 1.65 N RMS force on the level of M1, hence 0.55 N RMS wind force on a single PACT. The corresponding force spectrum, on the level of PACT, is shown in figure 6. This figure also shows the output spectrum of the fourth order linear filter (fed by random noise) which is used to simulate this wind spectrum.

Strictly speaking there is a dynamic transmissibility between forces on the surface of an M1 segment and forces on the PACT voice coil. However, it can be shown, using e.g. the analytic model discussed in Section 3.2, that this transmissibility is close to unity in the low-frequency range where wind forces are relevant. This effect is therefore neglected in the rest of this article.

4. FEEDBACK CONTROL

The feedback controller design for PACT comprises two parts: the high-performance fine stage controller design and the coarse stage design.

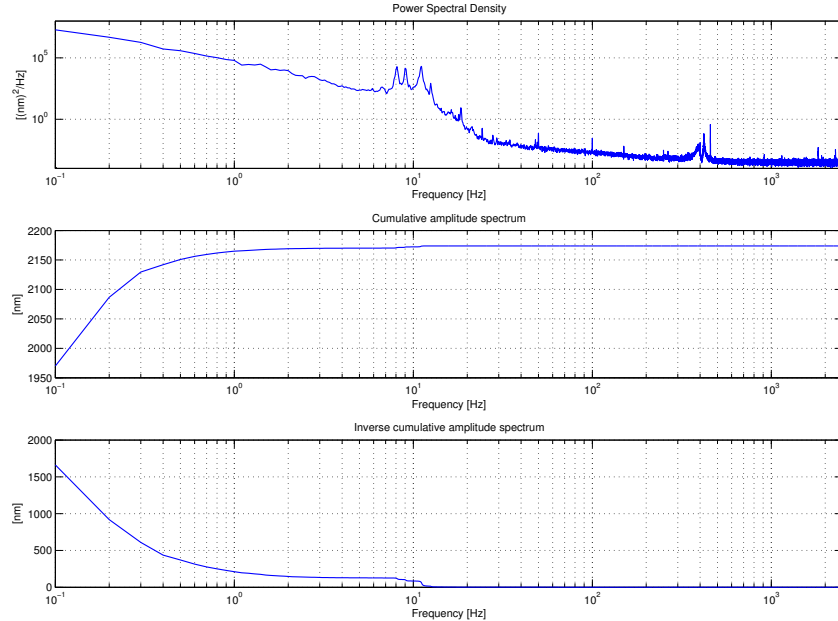


Figure 7: Open loop spectrum of the internal sensor signal in the presence of ground vibrations and wind forces; both the PSD (top), the left-integrated (middle) and right-integrated cumulative RMS (bottom) are shown.

4.1 Fine stage controller design

To make proper controller design trade-offs, an open loop power spectral density (PSD) plot of the error can be very useful. This PSD, as measured by the PACT internal sensor, in the presence of ground and wind disturbances, is shown in figure 7. The open loop error sums to more than 2000 nm RMS, which should eventually decrease to the required 1.7 nm.³

The fine stage controller has been constructed using a loopshaping design technique. Looking at the open-loop PSD a number of required controller features have been identified which should be incorporated in this design. Apart from containing a lead filter, which is needed to generate a phase lead in view of closed-loop stability, the controller should

- contain two integrators, to get rid of the low-frequency contribution of the wind forces;
- have a large gain (i.e. contain inverse notches) at 8.3 and 9.1 Hz, to suppress the specifically induced vibrations at these frequencies in closed loop;
- yield a high as possible bandwidth to suppress as many mid-range frequencies as possible;
- contain a low-pass filter, to filter out high-frequency noise sources.

Note that the peak at 11 Hz is not explicitly taken into account in the controller; it coincides with a resonance in the FRF (see figure 3(a)), so the plant itself already yields a large open-loop gain and resulting closed-loop suppression at that frequency.

At the same time the controller should be fairly robust. To this end a 6 dB modulus margin⁸ is formulated which should hold for all identified FRFs $H_i(j\omega)$ over the coarse stage stroke (see figure 3(a)), i.e.

$$|S_i(j\omega)| = \left| \frac{1}{1 + H_i(j\omega)C(j\omega)} \right| \leq 2 \quad \forall i, \quad (16)$$

where $C(j\omega)$ is the frequency response of the controller. Moreover, it has been decided not to completely cancel the 60 Hz anti-resonance by the low-pass filter poles, but to place the latter at a somewhat higher frequency. This way the controller is more robust for changes or uncertainties in this anti-resonance.

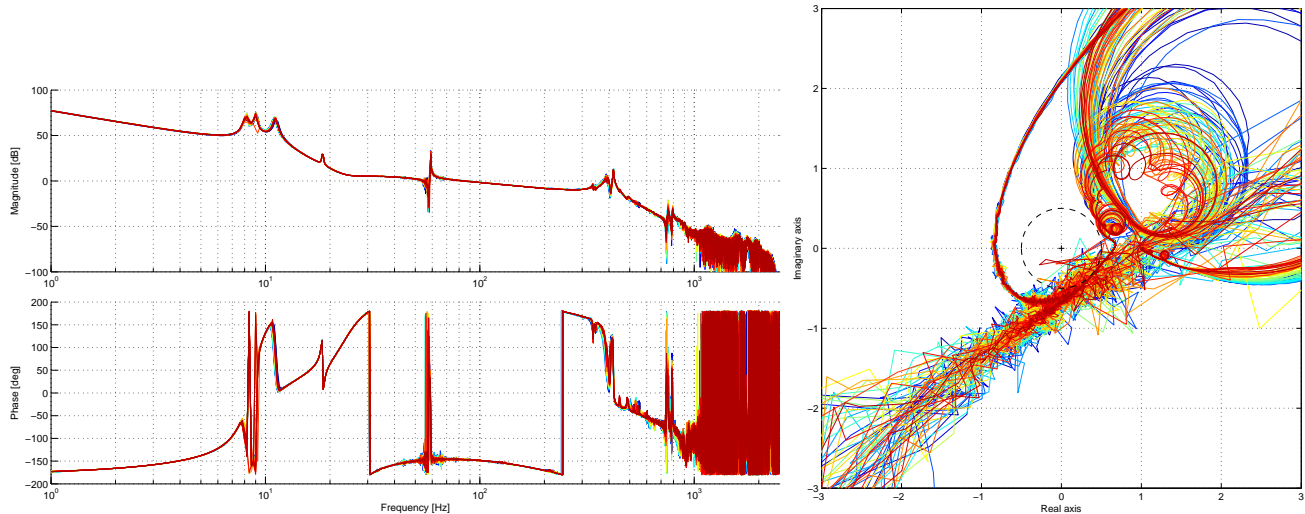


Figure 8: Open loop frequency response $H_i(j\omega)C(j\omega)$ both in a Bode diagram (left) and a Nyquist plot (right).

The performance and robustness of the final loopshaped controller design is represented in figure 8. This figure shows all open loops $H_i(j\omega)C(j\omega)$, both in a Bode plot and in a Nyquist diagram. The former shows that the obtained bandwidth, defined as the 0 dB crossover frequency of the open loop, is roughly between 54 Hz (first crossover) and 85 Hz (second crossover). The Nyquist plot proves that all loops are indeed closed-loop stable,⁸ since the point $(-1,0)$ is on the left-hand-side of all $H_i(j\omega)C(j\omega)$. The robustness is somewhat tricky to judge due to the bad coherence of the FRFs around the 60 Hz anti-resonance; however, looking through the accompanying measurement noise it can be concluded that on average all $H_i(j\omega)C(j\omega)$ remain outside the dashed disc with radius $\frac{1}{2}$ around the point $(-1,0)$, hence all loops are considered to satisfy the 6 dB robustness constraint (16).

4.2 Coarse stage controller design

To demonstrate the tracking performance of PACT over a significant part of the stroke, a coarse stage controller is also needed. This controller has to minimize the power consumption of the voice coil, which is directly linked to the voice coil force. Hence, it is suggested to use the control strategy as illustrated in figure 9. The top part of this diagram represents the fine stage loop discussed in Section 4.1, where the fine stage controller C_{VC} commands the voice coil actuated plant H_{VC} in order to let the PACT position y track the reference position y_{ref} . The accompanying voice coil force F_{VC} is taken as output for the (bottom) coarse stage loop, in which a to-be-designed controller C_{DC} commands a DC-motor velocity v_{DC} , affecting the PACT position y and thereby the required voice coil force.

The above approach effectively creates a MIMO (multiple-input-multiple-output) system, which in closed loop can have interaction between its inputs F_{VC} and v_{DC} and outputs y and F_{VC} . This can be dealt with by using a sequential loop closing^{8,9} approach. First, the high-bandwidth fine stage loop is closed, as discussed in

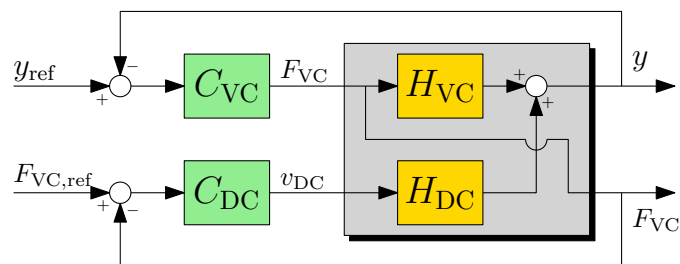


Figure 9: Block diagram of the combined fine and coarse stage control strategy.

Section 4.1, and the resulting equivalent plant H_{eq} for the coarse stage controller is determined as

$$H_{\text{eq}} = -\frac{C_{\text{VC}}}{1 + C_{\text{VC}}H_{\text{VC}}} \cdot H_{\text{DC}}. \quad (17)$$

The plant H_{DC} actually represents a local velocity control loop of the DC-motor. This local controller operates on the torque of the DC-motor with a fairly high bandwidth, so that the real velocity tracks the reference value v_{DC} . As such this velocity controller has a linearizing effect, since it removes the effect of dry and viscous friction to a large extent. As a result H_{DC} behaves like a simple integrator for low frequencies; since $\frac{C_{\text{VC}}}{1 + C_{\text{VC}}H_{\text{VC}}}$ is nearly constant for low frequencies, the same holds for the equivalent plant H_{eq} (a constant v_{DC} will result in a linearly increasing F_{VC}).

In the second loop closing step a low-bandwidth controller C_{DC} for this H_{eq} is tuned. In this case the coarse stage is mainly meant for low-frequent off-loading of the voice coil, hence C_{DC} can simply be a gain with a 2 Hz low-pass filter, resulting in a bandwidth well below 1 Hz. Since the bandwidths of the fine and coarse stage are so far apart, and the MIMO plant has actually a triangular structure (i.e. there is no open-loop transfer between v_{DC} and F_{VC}), interaction of the loops is minimized and MIMO stability can be guaranteed.⁸

4.3 Closed-loop tracking results

The above discussed fine and coarse stage controllers have been implemented and applied to PACT (mounted in its test setup, in horizontal configuration). While in closed loop, the actuator has been subjected to an E-ELT relevant scenario. To this end the position setpoint is initially constant, then increased to a constant tracking velocity³ of 1.2 $\mu\text{m/s}$, and then reversed with the same velocity in the opposite direction. This motion cycle lasts 900 s, thereby covering more than 500 μm stroke. The resulting closed-loop response as measured by the internal metrology, both in time and frequency domain, is depicted in figure 10.

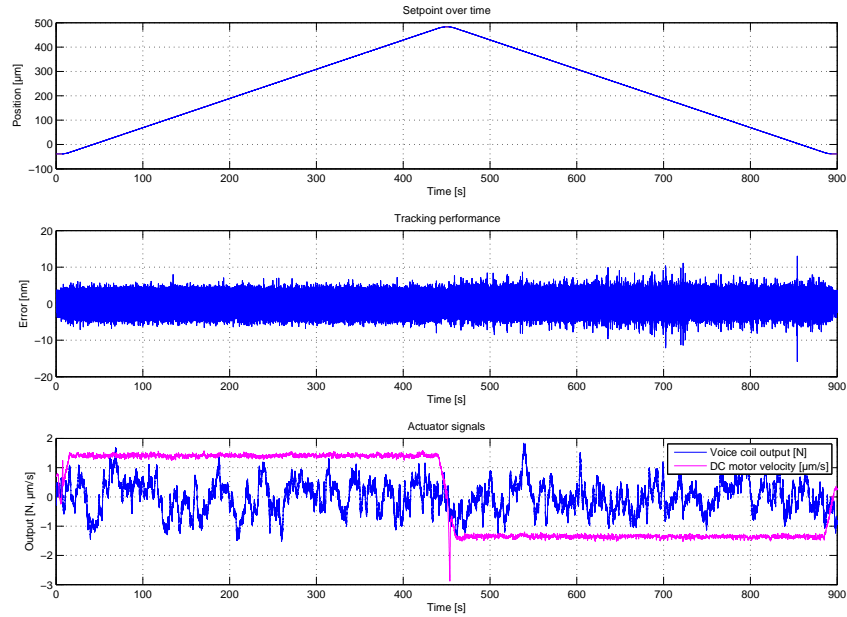
The time domain plot in figure 10(a) shows that the setpoint is accurately tracked well within ± 10 nm. The error is slightly larger in the backward ‘downhill’ motion than in the forward ‘uphill’ motion, which can be attributed to the self-locking behavior of the coarse stage. The voice coil force in the bottom plot clearly shows the compensation of the low-frequent wind disturbances. Still, this force nicely oscillates around zero, well within ± 2 N, due to the DC-motor off-loading with nearly constant velocity. Note that this DC-motor velocity is somewhat larger than the requested 1.2 $\mu\text{m/s}$; the coarse stage partly pushes against the PACT stiffness k_p , so that the effective internal sensor displacement is somewhat smaller than the coarse stage has moved.

The frequency domain representation of the measured error, depicted in figure 10(b), shows that the RMS error is only 1.4 nm, i.e. well within the requirement. This is roughly a factor $1.5 \cdot 10^3$ improvement compared to the open loop response. The PSD shows that the low-frequent wind contribution and the vibrations on 8.3 and 9.1 Hz are indeed very well suppressed. Some other peaks still remain, but the cumulative spectra prove that these peaks do not significantly contribute to the total RMS error. It is estimated that at least 0.5 nm of the obtained 1.4 nm can be attributed to sensor noise.

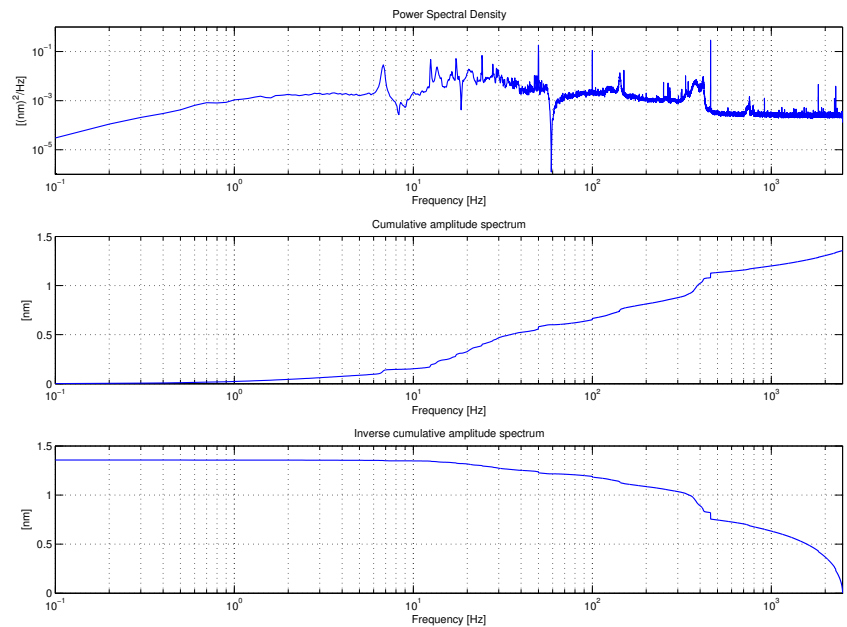
5. CONCLUSIONS

TNO has designed and realized various piston-tip-tilt actuator prototypes for the segmented primary mirror of large telescopes, in particular for the E-ELT. This paper has presented some recently obtained control results with one of these prototypes. To this end frequency response measurements have been taken and a first principles model of PACT in interaction with its test setup has been derived, with which the dynamics of the actuator has been assessed successfully. Next, a high-performance fine stage controller has been designed, using the PACT internal metrology as feedback sensor, and a low-bandwidth coarse stage controller has been derived for fine stage off-loading purposes. Finally, an E-ELT relevant tracking experiment has been presented, in the presence of both ground vibrations and wind disturbances, which has demonstrated the high performance of the feedback-controlled PACT, obtaining a position error of just 1.4 nm RMS, which is compliant with the requirements.

The attentive reader will note that the 1.7 nm accuracy requirement is at the level of PACT itself, being a relative measure between the fixed frame of the segment support and the PACT tip. This does not automatically imply the same positioning accuracy at M1 segment level. There is a significant amount of dynamics between



(a) In time domain; setpoint and output (top), tracking error (middle) and voice coil force and DC-motor velocity (bottom).



(b) In frequency domain; PSD of the error signal (top) and left- (middle) and right-integrated (bottom) cumulative RMS of the error.

Figure 10: Measured closed-loop tracking results.

PACT and the M1 segment surface, which can be excited even though the actuator is standing still. The decoupling of the M1 mass m_t with respect to the PACT moving mass m_p around the support structure stiffness k_s , associated with the 60 Hz anti-resonance and 400 Hz resonance, is particularly relevant in this regard. But also higher order modes will cause the segment to move relative to PACT.

Considering the aforementioned, the M1 segment positioning relative to the fixed frame could potentially be

improved by a modified controller design, most likely at the expense of a worse performance at PACT level. However, this still does not guarantee a good absolute positioning of a segment, i.e. relative to the sky. In the current baseline control approach any PACT closed loop will create a stiff connection between M1 segment and fixed frame; this is obviously beneficial for wind force attenuation, but frame vibrations are directly transferred to the segment. For this reason TNO is also investigating alternative control approaches, such as acceleration feedback,¹⁰ Kalman filtering or inferential control. Apart from this TNO continues to evaluate the different PACT prototypes, and aims to provide the best as possible position actuator, with accompanying control strategies, for segmented primary mirror telescopes.

APPENDIX A. SOME MODELING DETAILS

As mentioned in Section 3.2 all horizontal and vertical movement of the masses of the model represented in figure 4 can be expressed in terms of the generalized DOF $q = [x_p, x_t, y, \varphi]^T$. Assuming only small angles φ and displacements y , x_p and x_t , these expressions can be approximated by

$$\text{Box} : \begin{cases} \text{Hor} : (L - y) \sin \varphi \approx L\varphi \\ \text{Ver} : L - (L - y) \cos \varphi \approx y \end{cases} \quad (18a)$$

$$\text{PACT} : \begin{cases} \text{Hor} : (L - y) \sin \varphi - (\delta_p + x_p) \cos(\beta + \varphi) \approx L\varphi + \delta_p \varphi \sin \beta - x_p \cos \beta \\ \text{Ver} : L - (L - y) \cos \varphi - (\delta_p + x_p) \sin(\beta + \varphi) \approx y - \delta_p \varphi \cos \beta - x_p \sin \beta \end{cases} \quad (18b)$$

$$\text{Test mass} : \begin{cases} \text{Hor} : (L - y) \sin \varphi + (\delta_t - x_t) \cos(\beta + \varphi) \approx L\varphi - \delta_t \varphi \sin \beta - x_t \cos \beta \\ \text{Ver} : L - (L - y) \cos \varphi + (\delta_t - x_t) \sin(\beta + \varphi) \approx y + \delta_t \varphi \cos \beta - x_t \sin \beta \end{cases} \quad (18c)$$

These expressions can then be used to derive the kinetic energy T , potential energy V and their partial derivatives for substitution in the Lagrange equation (2). Hence (3) elaborates to

$$\begin{aligned} T \approx & \frac{1}{2} (m_b + m_p + m_t) (L^2 \dot{\varphi}^2 + \dot{y}^2) \\ & + \frac{1}{2} m_p [\delta_p^2 \dot{\varphi}^2 + \dot{x}_p^2 + 2L\dot{\varphi}^2 \delta_p \sin \beta - 2L\dot{\varphi} \dot{x}_p \cos \beta - 2\dot{y} \dot{\varphi} \delta_p \cos \beta - 2\dot{y} \dot{x}_p \sin \beta] \\ & + \frac{1}{2} m_t [\delta_t^2 \dot{\varphi}^2 + \dot{x}_t^2 - 2L\dot{\varphi}^2 \delta_t \sin \beta - 2L\dot{\varphi} \dot{x}_t \cos \beta + 2\dot{y} \dot{\varphi} \delta_t \cos \beta - 2\dot{y} \dot{x}_t \sin \beta], \end{aligned} \quad (19)$$

so that its derivatives become

$$\frac{d}{dt} (T, \dot{q}) = \begin{bmatrix} m_p \ddot{x}_p - m_p L \ddot{\varphi} \cos \beta - m_p \ddot{y} \sin \beta \\ m_t \ddot{x}_t - m_t L \ddot{\varphi} \cos \beta - m_t \ddot{y} \sin \beta \\ (m_b + m_p + m_t) \ddot{y} - m_p \delta_p \ddot{\varphi} \cos \beta - m_p \ddot{x}_p \sin \beta + m_t \delta_t \ddot{\varphi} \cos \beta - m_t \ddot{x}_t \sin \beta \\ (m_b + m_p + m_t) L^2 \ddot{\varphi} + (m_p \delta_p^2 + m_t \delta_t^2) \ddot{\varphi} + 2L(m_p \delta_p - m_t \delta_t) \ddot{\varphi} \sin \beta \\ - m_p L \ddot{x}_p \cos \beta - m_t L \ddot{x}_t \cos \beta - \ddot{y} (m_p \delta_p - m_t \delta_t) \cos \beta \end{bmatrix} \quad (20a)$$

$$T, q = [0 \ 0 \ 0 \ 0]^T \quad (20b)$$

Similarly, (4) elaborates to

$$\begin{aligned} V = & \frac{1}{2} k y^2 + \frac{1}{2} k_p x_p^2 + \frac{1}{2} k_t x_t^2 + \frac{1}{2} k_s (x_p - x_t)^2 + (m_b + m_p + m_t) g [L(1 - \cos \varphi) + y \cos \varphi] \\ & - m_p g (\delta_p + x_p) \sin(\beta + \varphi) + m_t g (\delta_t - x_t) \sin(\beta + \varphi), \end{aligned} \quad (21)$$

so that its derivative can be approximated by

$$V, q \approx \begin{bmatrix} (k_p + k_s) x_p + k_s x_t - m_p g \varphi \cos \beta \\ (k_t + k_s) x_t + k_s x_p - m_t g \varphi \cos \beta \\ k y \\ (m_b + m_p + m_t) g L \varphi + g \varphi (m_p \delta_p - m_t \delta_t) \sin \beta - m_p g x_p \cos \beta - m_t g x_t \cos \beta \end{bmatrix}. \quad (22)$$

Substitution of the expressions (20a), (20b), (22) and the non-conservative forces $Q^{nc} = [F, 0, 0, 0]$ into (2) then yields the equations of motion for the complete setup, i.e.

$$m_p \ddot{x}_p - m_p L \ddot{\varphi} \cos \beta - m_p \ddot{y} \sin \beta + (k_p + k_s)x_p - k_s x_t - m_p g \varphi \cos \beta = F \quad (23a)$$

$$m_t \ddot{x}_t - m_t L \ddot{\varphi} \cos \beta - m_t \ddot{y} \sin \beta + (k_t + k_s)x_t - k_s x_p - m_t g \varphi \cos \beta = 0 \quad (23b)$$

$$(m_b + m_p + m_t) \ddot{y} - m_p \delta_p \ddot{\varphi} \cos \beta - m_p \ddot{x}_p \sin \beta + m_t \delta_t \ddot{\varphi} \cos \beta - m_t \ddot{x}_t \sin \beta + ky = 0 \quad (23c)$$

$$\begin{aligned} & (m_b + m_p + m_t) L^2 \ddot{\varphi} + (m_p \delta_p^2 + m_t \delta_t^2) \ddot{\varphi} + 2L(m_p \delta_p - m_t \delta_t) \ddot{\varphi} \sin \beta \\ & - m_p L \ddot{x}_p \cos \beta - m_t L \ddot{x}_t \cos \beta - \ddot{y}(m_p \delta_p - m_t \delta_t) \cos \beta \\ & + (m_b + m_p + m_t) g L \varphi + g \varphi (m_p \delta_p - m_t \delta_t) \sin \beta - m_p g x_p \cos \beta - m_t g x_t \cos \beta = 0. \end{aligned} \quad (23d)$$

By writing this in the form of (5) the matrices M and K as defined in (6) and (7) follow automatically.

REFERENCES

- [1] Jared, R. C., Arthur, A. A., Andraea, S., Biocca, A. K., Cohen, R. W., Fuertes, J. M., Franck, J., Gabor, G., Llacer, J., Mast, T. S., Meng, J. D., Merrick, T. L., Minor, R. H., Nelson, J. T., Orayani, M., Salz, P., Schaefer, B. A., and Witebsky, C., "The W.M. Keck telescope segmented primary mirror active control system," *Proc. SPIE* **1236**, 996–1008 (1990).
- [2] Kamphues, F., Nijenhuis, J. R., den Breeje, R., van den Dool, T. C., and Ponsioen, J., "PACT: the actuator to support the primary mirror of the ELT," *Proc. SPIE* **7018**, 70180Z (2008).
- [3] Erm, T., "Technical specification for the manufacturing and delivery of prototype position actuators for the primary mirror of the European Extremely Large Telescope (E-ELT)," Tech. Rep. E-SPE-ESO-142-0011, issue 2, ESO (2009).
- [4] de Kraker, A., [*Mechanical Vibrations*], Shaker Publishing, Maastricht, NL (2009).
- [5] Koehler, B., "E-ELT environmental conditions," Tech. Rep. E-SPE-ESO-313-0111, issue 5, ESO (2012).
- [6] ESDU 85020, *Characteristics of atmospheric turbulence near the ground. Part II: single point data for strong winds*. Engineering Sciences Data Unit, London, UK (1985).
- [7] Tomasini, G. and Cheli, F., "Admittance function to evaluate aerodynamic loads on vehicles: Experimental data and numerical model," *Journal of Fluids and Structures* **38**, 92–106 (2013).
- [8] Skogestad, S. and Postlethwaite, I., [*Multivariable Feedback Control: analysis and design*], John Wiley, Chichester, UK (2005).
- [9] Hovd, M. and Skogestad, S., "Sequential design of decentralized controllers," *Automatica* **30**(10), 1601–1607 (1994).
- [10] Sedghi, B., Bauvir, B., and Dimmler, M., "Acceleration feedback control on an AT," *Proc. SPIE* **7012**, 70121Q–1 (2008).